Journal of
Manufacturing and Materials Processing

MDPI

Article

Effect of Post-Processing on the Microstructure of WE43 Magnesium Alloy Fabricated by Laser Powder Directed Energy Deposition

Leila Sorkhi [1], Nathan J. Madden [1] and Grant A. Crawford [1,2,*]

[1] Arbegast Materials Processing and Joining Laboratory, South Dakota School of Mines & Technology, 501 E. Saint Joseph St., Rapid City, SD 57701, USA; leila.sorkhi@sdsmt.edu (L.S.); nathan.madden@sdsmt.edu (N.J.M.)
[2] Materials and Metallurgical Engineering Department, South Dakota School of Mines & Technology, 501 E. Saint Joseph St., Rapid City, SD 57701, USA
* Correspondence: grant.crawford@sdsmt.edu; Tel.: +1-605-394-5133

Abstract: Additive manufacturing of magnesium (Mg) alloys is of interest for the fabrication of complex-shaped lightweight materials. This study evaluates the microstructure of WE43 Mg alloy deposited using laser powder directed energy deposition (LPDED) additive manufacturing technique in as-deposited and post-processed conditions. As-deposited samples exhibited roughly 2% porosity, which was reduced to below 0.1% after hot isostatic pressing. Despite limited grain growth after heat treatment, some grains experienced abnormal grain growth, likely due to Zener pinning and non-uniform dissolution of grain boundary precipitates. Moreover, as-deposited specimens contained Nd-rich grain boundary precipitates which dissolved during post-processing. Additionally, during heat treatment. a fine distribution of needle-like β1 or β precipitates formed. Overall, the precipitate size and distribution following heat treatment was non-uniform, likely because of the non-uniform response of the LPDED material to heat treatment, owing to the variation in local- and global-temperature profiles during deposition. Furthermore, arc-shaped phases with a high concentration of Y, O, and Zr were present for all processing conditions and are associated with the passivation of the feedstock powder prior to deposition. Moreover, an equiaxed-grain structure with a random orientation and a finer grain size in the regions adjacent to the arc-shaped phases was observed in all processing conditions.

Keywords: additive manufacturing; laser powder directed energy deposition; magnesium; microstructure; post-processing

Academic Editor: Chao Yang

Received: 1 December 2024
Revised: 20 December 2024
Accepted: 25 December 2024
Published: 26 December 2024

Citation: Sorkhi, L.; Madden, N.J.; Crawford, G.A. Effect of Post-Processing on the Microstructure of WE43 Magnesium Alloy Fabricated by Laser Powder Directed Energy Deposition. *J. Manuf. Mater. Process.* **2025**, *9*, 3. https://doi.org/10.3390/jmmp9010003

1. Introduction

Recently, magnesium (Mg) and Mg alloys have gained considerable attention for use as biodegradable implants [1–5] because of its natural degradation in the physiological environment and being an essential nutritional element (240–420 mg/day) [1,3] for maintaining proper bodily function. Furthermore, Mg has an elastic modulus (41–45 GPa) that more closely matches that of human bone (15–25 GPa), which is expected to limit stress shielding (a process by which stiffness mismatch between the implant and bone can result in bone resorption). Widespread adoption of biodegradable Mg implants, however, has been limited because the corrosion rate of Mg in the body is too rapid (often resulting in uncontrolled hydrogen gas evolution), and Mg alloys have poor formability [1,2,5–8].

Efforts to manufacture biodegradable Mg-based implants have primarily employed casting or powder metallurgy techniques which, in most cases, permits the fabrication of

complex geometries. Recently, however, additive manufacturing (AM) of Mg alloys has gained interest for the potential to manufacture unique complex geometries, unachievable by conventional manufacturing methods, to decrease material waste or provide functional design options for aerospace, automotive, and biomedical applications [9–12]. AM is a relatively new manufacturing method that fabricates parts in a layer-by-layer fashion. While there are a variety of AM technologies, powder bed fusion (PBF) and directed energy deposition (DED) are two of the most commonly employed for the manufacturing of metals. While metal AM is now well-established for many ferrous, titanium, and nickel alloys (among others), AM of Mg is much less established. The lack of activity is likely associated with two primary challenges: (a) the high oxygen affinity and pyrophoric nature of Mg (particularly in powder form), presenting both a process challenge and safety risk, and (b) a limited process window due to a small difference in melting temperature (~640 °C) and vaporization temperature (~1100 °C) [9,10,13,14].

Nevertheless, over the past decade, the interest in Mg AM has increased and several published reports now exist [9–11,13,15–30]. The vast majority of these efforts have employed PBF methods [9,10,15–18,20,25–27]. Ng et al. [16] reported on the melting of fine Mg powder using a miniature PBF system that was enclosed by a custom inert-gas (argon) chamber, to prevent oxidation [16]. More recently, Gangireddy et al. [20] reported a reduction in porosity in WE43 Mg fabricated via PBF after hot isostatic pressing (HIP), where mechanical properties were strongly influenced by the degree of porosity in the specimen. Moreover, the authors reported on the microstructural evolution of various second-phase particles (e.g., yttrium(Y)- and zirconium(Zr)-rich oxides and $Mg_{24}Y_5$ and Nd-rich precipitates) in the as-built and HIP conditions [20]. Furthermore, Esmaily et al. [29] reported the microstructure of WE43 Mg alloy specimens fabricated using SLM, consisting of refined grains with irregular morphologies and a strong basal texture with *c*-axis parallel to the build direction. Moreover, secondary processing, including HIP, as well as heat treatment, resulted in insignificant grain growth and the grain texture remained unchanged. Also, although post-processing lead to the dissolution of Nd- and Y- rich particles, the flake-shaped oxide particles were retained [29].

To the authors' knowledge, there are only a limited number of publications on the use of laser powder DED (LPDED) for AM of Mg [17,19,28,30]. Tandon et al. evaluated [17,19] the microstructure and mechanical properties of LPDED WE43 Mg specimens with low porosity (~99% density). The authors reported that post-deposition T6 heat treatment and HIP treatment improved the mechanical behavior of the deposited samples compared to the as-deposited condition. Jiang et al. [28] also utilized the DED method to deposit Mg-xGd-3Y-0.2Zr alloys and studied the effects of Gd addition on microstructure and mechanical properties of the deposited samples [28]. However, in-depth microstructure characterization was not provided in any of these published works.

In our previous paper [30], we have studied the effect of interlayer interval time on the microstructure and mechanical properties (microhardness and uniaxial tensile) of the WE43 specimens deposited using the LPDED method. The results showed that despite the insignificant effect of interlayer interval time on the microstructure of the deposited samples in various post-processing conditions, the tensile strength and ductility of the specimens significantly decreased by increasing interlayer interval time, due to the presence of lack-of-fusion defects. Moreover, post-processing (e.g., heat treatment and HIP) improved yield strength, ultimate tensile strength, and ductility of the specimens in both processing conditions. However, the influence of post-deposition heat-treatment on the microstructure of additively manufactured Mg was not investigated in our previous study [30] or elsewhere. Considering that most additively manufactured Mg alloys will be post-processed prior to service, it is critical to understand the influence of heat treatment

and HIP on the microstructure of the specimens. In this work, the microstructure of WE43 Mg alloy specimens fabricated using LPDED is investigated. Also, the effect of HIP and heat-treatment on the microstructure of additively manufactured specimens is investigated.

2. Materials and Methods

Rectangular (10.8 × 48.0 × 114.3 mm) WE43 magnesium alloy specimens (Figure 1) were fabricated using a modified laser-engineered net shaping (LENS®) system. All samples were processed on wrought WE43 substrates (ELEKTRON® 43 rolled plate, Magnesium Elektron, Flemington, NJ, USA) using a gas-atomized WE43 powder (Elektron® MAP+43, Magnesium Elektron, Flemington, NJ, USA) with a nominal composition of Mg, 3.97 wt.% Y, 2.23 wt.% Nd, and 0.59 wt.% Zr and a particle size of 68.9 ± 13.5 µm (determined via laser diffraction particle analysis (LDPA)). Samples were fabricated using the line-melting contours with snaking fill technique and the LPDED process conditions listed in Table 1. Considering the pyrophoric nature of the Mg powder and to prevent excessive oxidation, all specimens were processed in an argon atmosphere while keeping oxygen content lower than 100 ppm.

To evaluate the influence of post-processing on the microstructure of the as-deposited material, both heat treatment and hot isostatic pressing (HIP) were performed. As such, this study evaluated samples prepared in four conditions: as-deposited (AD), heat-treated only (HT), HIP only (HIP), and HIP and heat-treated (HIP + HT). Heat treatment was performed using a standard T6 heat-treatment process for WE43: solution treatment at 525 °C for 8 h, followed by quenching in water and aging at 250 °C for 16 h and air cooling [31]. All heat treatments were performed in air atmosphere in a box furnace (Lindberg/Blue, Thermo Scientific, Waltham, MA, USA). HIP was performed at Quintus Technologies, LLC (Lewis Center, OH, USA) and the process conditions were 520 °C for 2 h at a pressure of 100 MPa.

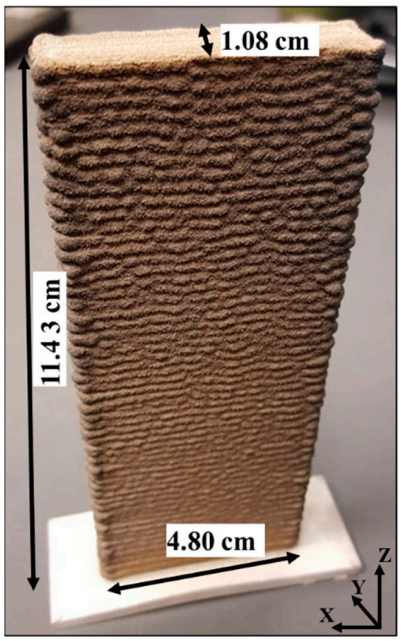

Figure 1. Image of the as-built rectangular WE43 magnesium alloy specimen produced by LPDED. Z-direction represents build direction.

Table 1. LPDED processing conditions.

Laser Power (W)	Contour Traverse Speed (mm/s)	Hatch Traverse Speed (mm/s)	Layer Height (mm)	Powder Feed Rate (rpm)	Hatch Distance (mm)
600	19.05	12.7	0.508	2.8	1.12

To study the size and morphology of the as-received powder, a small amount of powder was sprinkled on carbon tape and evaluated using scanning electron microscopy (SEM) (Supra 40 VP, Zeiss, Germany). Also, energy-dispersive X-ray spectroscopy (EDS) was conducted on cross-sectional samples to characterize the compositional variation within the powder particles. Metallographic preparation of both powder and additively manufactured specimens was performed by mounting the specimens in conductive epoxy resin, grinding with 1200 grit SiC paper, and polishing using 9 and 1 µm diamond suspensions. Final polishing was conducted using a 0.05 µm alumina powder suspension. All metallographic analysis was performed on the Z-Y plane (Figure 1). In the case of powder cross-sections, the surface was coated with a thin (~10 nm) layer of carbon to prevent charge accumulation on the sample surface owing to the epoxy mounting resin. Porosity analysis was performed based on ASTM standard E2109 [32], using optical microscopy (Axio Vert.A1 inverted microscope, Carl Zeiss Microscopy GmbH, Germany) in conjunction with image analysis (ImageJ, National Institutes of Health (NIH)). For this purpose, 10 optical micrographs were collected using a magnification of 200×. Etched samples were etched in a solution containing 60 mL ethylene glycol, 20 mL acetic acid, 19 mL water, and 1 mL nitric acid [33]. The microstructure and grain size of the etched samples were characterized using optical microscopy. The grain size was measured using the line-intercept method on 10 different images with five distinct lines in both vertical and horizontal directions, and the diameter of the grains was calculated based on the ASTM E112 [34].

Cross-sectional SEM and EDS analysis was performed on the AD and post-processed specimens to evaluate the microstructure and microscale composition. In all cases, cross-sectional characterization was performed on the Z-Y plane of the rectangular specimen (Figure 1). In addition, transmission electron microscopy [35] analysis (imaging and selected area diffraction pattern (SAED)) was conducted using a JEOL JEM-2100 LaB_6 TEM. Bright-field imaging and SAED were used to characterize the second-phase particle size, distribution, and type. In addition, the crystal structure of the as-received powder and additively manufactured materials was characterized via X-ray diffraction (XRD), using a Rigaku Ultima-Plus X-ray Diffractometer equipped with a CuKa X-ray source. The 2θ values varied from 10° to 90° at a scan rate of 2 degree/min.

Furthermore, the electron backscatter diffraction (EBSD) method was used to study the microstructure of the samples in various conditions. EBSD analysis was performed using an Oxford Aztec EBSD system in conjunction with SEM. The step size for each sample was set at 0.4 µm. Prior to EBSD, the samples were ground and polished with the abovementioned procedure. Then, the surface of the samples was milled using an ion beam milling system (EM TIC 3X, Leica, US) with the beam setting of 7 kV and 2.6 mA, for 5 h. To avoid the excessive heating of the samples during the ion milling process, the cryogenic cooling stage operating at −120 °C was used. Moreover, the Transmission Kikuchi Diffraction (TKD) method was also used to obtain further information on the microstructure of the various samples. TKD analysis was performed using the Oxford Aztec (Oxford Instruments NanoAnalysis, High Wycombe, UK) EBSD system with the Symmetry S2 detector in the SEM (Helios 5 CX DualBeam, ThermoFisher Scientific, Waltham, MA, USA) with a step size of 50 nm and 45.9 ms exposure time. For this purpose, cross-section lamellae were prepared using a DualBeam focused ion beam (FIB)- SEM (Helios 5 CX, ThermoFisher Scientific,

Waltham, MA, USA). A 2 μm thick protective tungsten layer was deposited prior to rough trenching with 30 kV Ga^+ at 0.79 nA. Trenching clean-up was conducted with 30 kV Ga^+ at 9.3 nA. Final lamellae thinning was performed at an ion beam current of 0.79 nA, and final polishing was conducted at 5 kV and 1 kV, to reduce FIB surface damage. The Mg FIB lamella was also used to study the chemistry of some of the samples, using EDS. The Oxford Instruments Ultim Max 100 EDS detector was used to collect EDS maps, using a 30 keV accelerating voltage with a 1.4 nA electron beam current.

3. Results

3.1. Powder Characterization

Figure 2 shows SEM images of the as-received powder. Powder particles were characterized by a near-spherical morphology and, in many cases, small satellite particles were observed attached to larger particles. The surface of the particles was characterized by a fine cellular structure, which is a result of rapid solidification during gas atomization. The WE43 powder had an average diameter of 68.9 ± 13.5 μm (determined by LDPA). Moreover, D10, D50, and D90 of the powder are determined as 47.3, 61.75, and 83.8 μm, respectively.

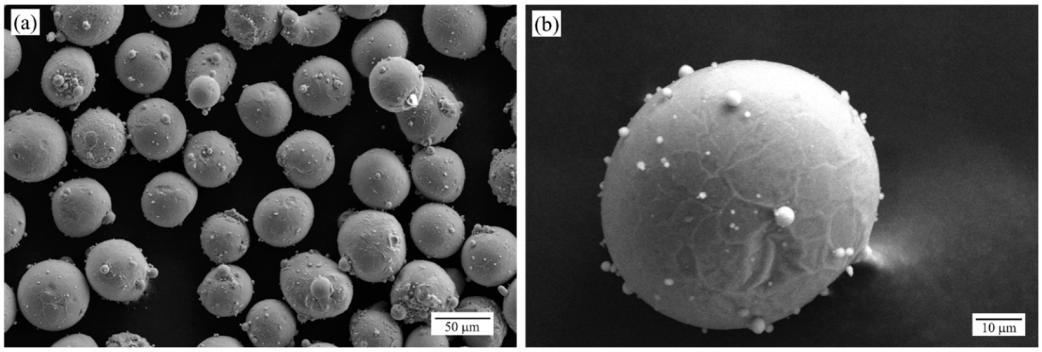

Figure 2. (**a**) Low magnification and (**b**) high magnification SEM images depicting the morphology of the gas-atomized WE43 Mg alloy powder.

Figure 3 shows cross-sectional SEM images and associated EDS elemental maps obtained from the interior of a typical powder particle. A fine cellular structure is apparent, whereby the cell boundaries appear bright due to elemental segregation that has occurred during solidification. It should be noted that due to the nature of the gas-atomized powder, although not significant, the cellular microstructure near the surface of the powder (Figure 3c) is finer than the central region (Figure 3a) because of the higher cooling rates experienced in the area near the surface of the powder.

Based on the EDS results (Figure 3b), the cell boundaries (bright regions) are rich in alloying elements including yttrium (Y), neodymium (Nd), and zirconium (Zr). Previous studies have concluded that the cell boundary regions likely contain the eutectic phase [36]. From inspection of Figure 3c,d, a thin layer (white arrow) rich in Y and oxygen (O) is present on the perimeter of the powder. This oxide layer is attributed to passivation of the Mg powders, which is carried out during production to ensure safe handling [36]. Moreover, comparing the EDS maps in Figure 3b,d, the cell boundaries in Figure 3b appear to be brighter in color as a result of the thicker cell boundaries. This difference in cell boundary thickness can be attributed to the lower cooling rates at the center of the powder particles, which allow for greater segregation of the alloying elements.

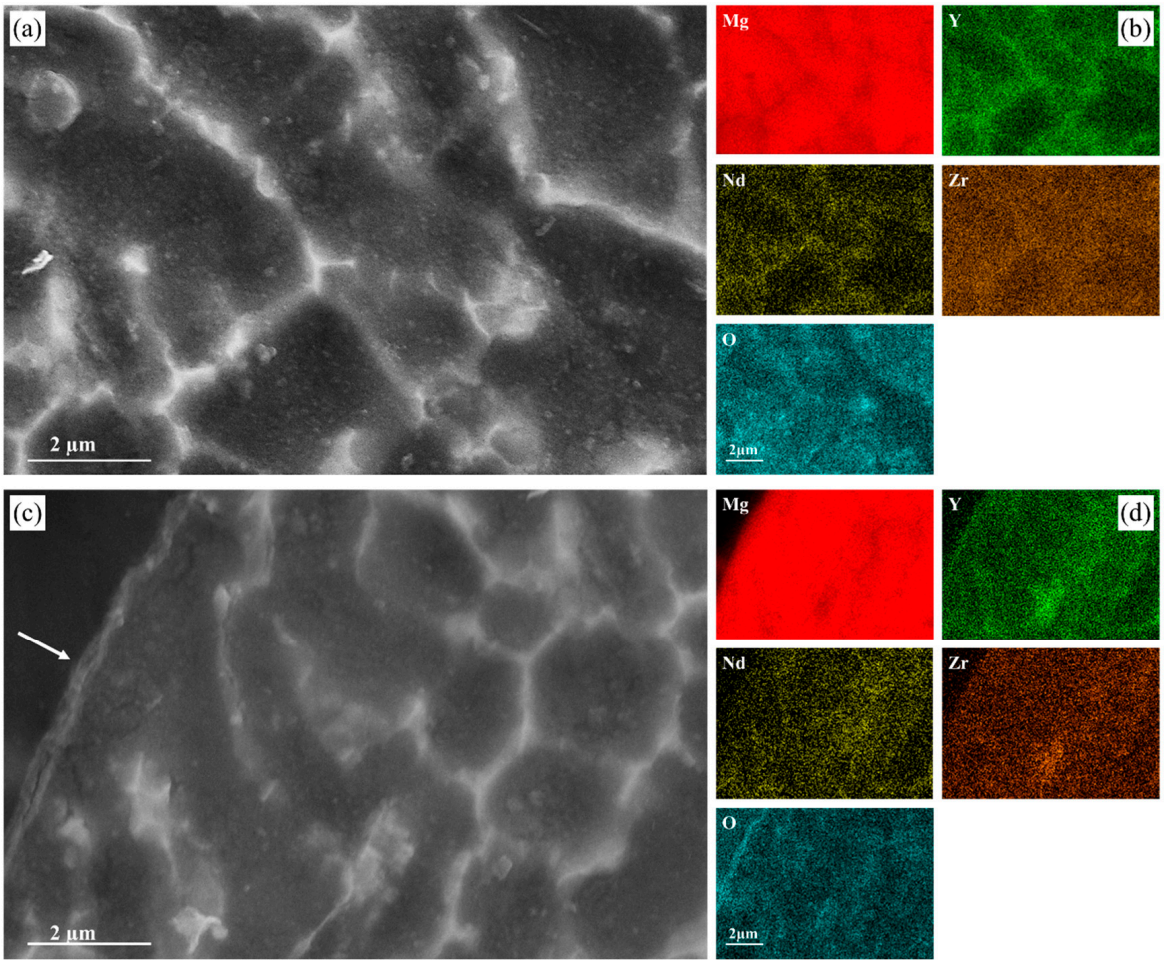

Figure 3. (**a**,**c**) SEM cross-sectional micrograph and (**b**,**d**) corresponding EDS elemental maps obtained from gas-atomized WE43 Mg powder. The white arrow marks the passive layer on the surface of the powder.

3.2. Microstructure Characterization

Figure 4 shows optical micrographs of the LPDED deposited WE43 material in AD, HT, HIP, and HIP + HT condition. In addition, Table 2 shows the measured porosity and grain size for the samples in each condition. From inspection of Figure 4, the AD material is characterized by a fine distribution of equiaxed grains and arc-shaped phases (red arrows). While the exact nature of these arc-shaped phases is not known, previously [19], they have been attributed to the passive oxide layer on the feedstock powder. These phases will be discussed in more detail using the EDS analysis. Moreover, gas porosity is also observed in the AD sample (blue arrows in Figure 4a).

Table 2. The porosity and grain size of LPDED WE43 Mg specimens in as-deposited and post-processed conditions.

Sample Condition	Porosity (% by Area)	Grain Diameter (µm)
AD	1.12 ± 0.36	10.6 ± 2.2
HT	1.52 ± 0.67	12.4 ± 2.0
HIP	0.01 ± 0.01	13.4 ± 3.1
HIP + HT	0.02 ± 0.01	15.5 ± 3.6

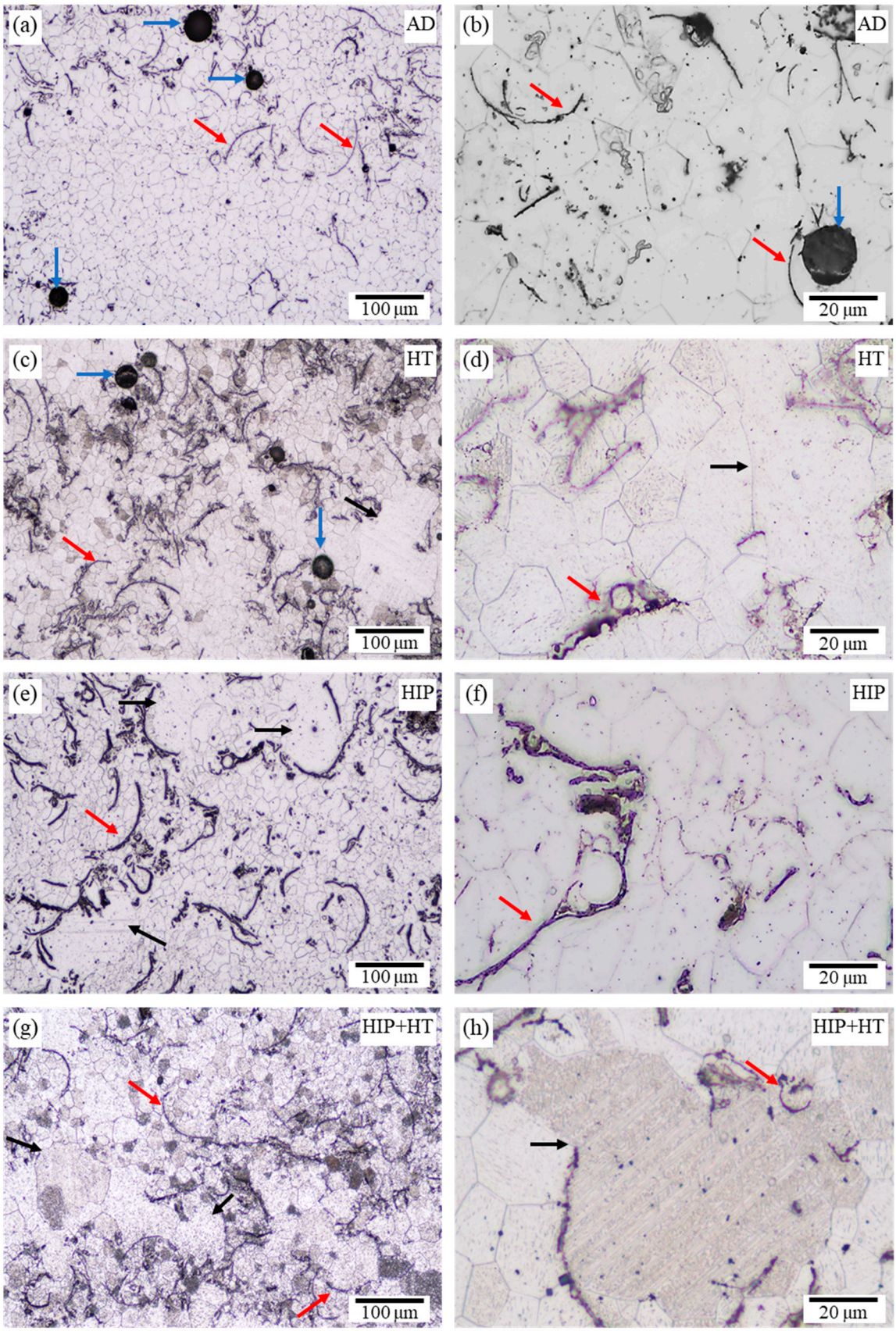

Figure 4. Cross-sectional optical micrographs of additively manufactured WE43 Mg in (**a**,**b**) AD, (**c**,**d**) HT (**e**,**f**) HIP, and (**g**,**h**) HIP + HT conditions. The blue arrows mark gas porosity. The black arrows point to the grains which grow distinctively. The red arrows mark the powder boundaries.

Heat treatment and HIP of the AD specimens resulted in several changes to the microstructure. First, the grain size increased for all post-treated LPDED specimens compared to the AD material. The increase in grain size was simply attributed to modest grain growth that occurred during elevated-temperature heat treatment. In addition, abnormal grain growth (AGG) was observed in the HT, HIP, and HIP + HT conditions, whereby some grains experienced significant grain growth. Black arrows shown in Figure 4 indicate large grains that have experienced AGG, surrounded by smaller equiaxed grains. Qualitative analysis indicated that the HIP + HT specimen experienced the largest amount of AGG, followed by the HT specimen. Furthermore, an increase in grain size variation was observed for the heat-treated specimens, which is attributed to the increase in AGG.

In general, grain growth occurs by two modes: normal grain growth and AGG [37]. During AGG, grain growth is discontinuous and a few grains grow at the expense of smaller grains, ultimately resulting in a bimodal grain size distribution [37]. AGG has been observed in numerous alloy systems and has been attributed to a variety of mechanisms including second-phase particle pinning (Zener pinning) [37–39], texture effects [39–41], and dislocation density gradients [42,43]. Among these mechanisms, the most commonly cited is the influence of second-phase particles on grain growth characteristics. More specifically, when annealing at high temperatures, non-uniform dissolution of grain boundary precipitates will frequently cause AGG [38]. As such, it is possible that AGG in this study has occurred because the AD microstructure was characterized by significant grain boundary precipitation (see Figure 4 and related discussion) and these precipitates rapidly underwent non-uniform dissolution during either the HIP treatment (HIP sample) or solution treatment (HT and HT+HIP samples). Because the process was non-uniform—possibly due to variations in the size and composition of the grain boundary precipitates formed during deposition—some grains experienced rapid AGG until all grain boundary precipitates were fully dissolved. Roostaei et al. [44] studied the grain growth kinetics of several Mg alloys and showed that when conditions are favorable for AGG, increased time at temperature increased the amount of AGG. Thus, it is reasonable that the HIP + HT specimen experienced the most AGG.

Compared to the AD condition, heat treating and/or HIP treatment did not remove the large arc-shaped phases. This is not surprising, considering the thermal stability of yttria (melting temperature = 2342 °C). Furthermore, from inspection of Table 2, three important observations can be made regarding the porosity of the specimens. First, the AD specimens exhibited porosity of less than 2%, which demonstrates the potential for successfully fabricating Mg components using LPDED. Second, HIP was effective in reducing the porosity to below 0.1%. This can be observed by comparing measured porosity (Table 2) for the AD and HT to the HIP and HIP + HT specimens. Similarly, optical micrographs provided in Figure 4 show that the porosity is primarily spherical in shape (likely gas porosity) and observed only in AD and HT samples. Third, the application of heat treatment resulted in a two-fold increase in porosity. This observation can be made by comparing either the AD and HT samples or the HIP and HIP + HT, although the total porosity was considerably lower for the HIP specimens. The presence of porosity in AD and HT samples can be attributed to gas entrapment during the LPDED process. Moreover, the feedstock powder contained significant gas porosity and is the most likely source for gas porosity in the AD and HT conditions. The reason for increased porosity following heat treatment could be associated with a metallographic preparation artifact, whereby the precipitates that have been formed during heat treatment are pulled out during mechanical polishing. Alternatively, the increase in porosity could be associated with the growth of gas pores during heat treatment. Although the gas pores collapse during HIP treatment, residual argon gas (present due to the low diffusivity of argon in Mg) near the original pores may

coalesce during subsequent heat treatment. This mechanism has been cited as a cause for increased porosity following heat treatment of additively manufactured titanium in HIP condition [45]. A similar mechanism could also occur for the HT sample if residual argon gas or small gas pores coalesce during heat treatment. Nevertheless, further studies are required to study the change in as porosity following heat treatment.

Figure 5 shows cross-sectional SEM micrographs of LPDED samples in various conditions (AD, HT, HIP, and HIP + HT). From inspection of Figure 5a,b, the AD sample contains small precipitates (bright regions) located along the α-Mg grain boundaries with limited second-phase particles located within the α-Mg grains. The grain boundary precipitates dissolved into the matrix after HIP or HT, although for heat-treated specimens (HT and HIP + HT) new grain boundary precipitates formed during aging. Note, the grain boundaries in the HIP-only specimen are poorly defined and show limited (if any) grain boundary precipitation. Once again, the AD and post-processed specimens (HT, HIP, HIP + HT) contain many arc-shaped phases (red arrows in Figure 5), which remained in the microstructure following post-processing. Moreover, comparing the microstructure of the heat-treated samples (i.e., HT and HIP + HT, Figures 5c and 5g, respectively) to those without heat treatment (i.e., AD and HIP, Figures 5a and 5e, respectively) shows the formation of small needle-like precipitates (yellow arrows in Figure 5d,h) after heat treatment. Based on the literature [46,47], these needle-like precipitates are likely β_1 precipitates which grow on the prismatic planes of the HCP lattice, perpendicular to the basal plane, and in the $[11\bar{2}0]$ direction. To evaluate the size, morphology, and distribution of these precipitates in more detail, TEM was conducted on the HIP + HT sample (discussed below). EDS analysis was performed to provide a qualitative description of the chemical composition of the secondary phases within the microstructure. Figure 6 shows SEM images and corresponding EDS elemental maps from various regions of the HT sample. The results show the arc-shaped phases (red arrows in Figure 6 exhibit a high concentration of Y, Zr, and O, while the Mg concentration is depleted in these regions. Therefore, these phases are likely oxides originating from the surface passivation treatment imposed on the Mg powder during processing, to ensure safe handling. The thickness of the arc-shaped phases in the LPDED samples is greater than that of the original surface oxide layer (Figure 3a), which could be attributed to surface oxidation during deposition or thickening of the layer within the melt pool. In addition, unlike the passivation layer on the as-received powder, the arc-shaped phases are enriched in Zr, suggesting that another process, beyond surface passivation, may have influenced their formation. As such, further investigation is necessary to fully understand the origin and evolution of these precipitates.

Figure 6a also reveals the presence of small cuboidal (yellow arrows) and some irregular precipitates (white arrow) in the microstructure of the HT sample, which did not dissolve during heat treatment. These precipitates were observed in all LPDED samples, regardless of the post-processing condition. The elemental map provided in Figure 6a indicates that the irregular precipitates are Zr-rich. Additionally, the higher-resolution SEM image and associated EDS elemental map provided in Figure 6b show that the cuboidal precipitates are rich in Y and also exhibit an elevated Zr content, compared to the average composition. Various compositions have been reported in the published literature for cuboidal Y-rich precipitates in WE43 (e.g., $Mg_{24}Y_5$, Mg_2Y [48], $Mg_3(Y_{16.49}\ Nd_{0.51})$ [49], and Y_7Zr [50]). Using EDS point analysis, we estimated the composition of the cuboidal precipitate to be 51.4 at.% Y, 36.3 at.% Mg, 2.9 at.% Nd, 2.3 at.% Dy, 1.2 at.% Gd, and 5.7 at.% O). Considering the limitations (e.g., spatial resolution) of this type of analysis, it is reasonable to infer that the cuboidal phase is rich in Y but also contains a mixture of rare-earth elements, which is not consistent with previously observed compositions.

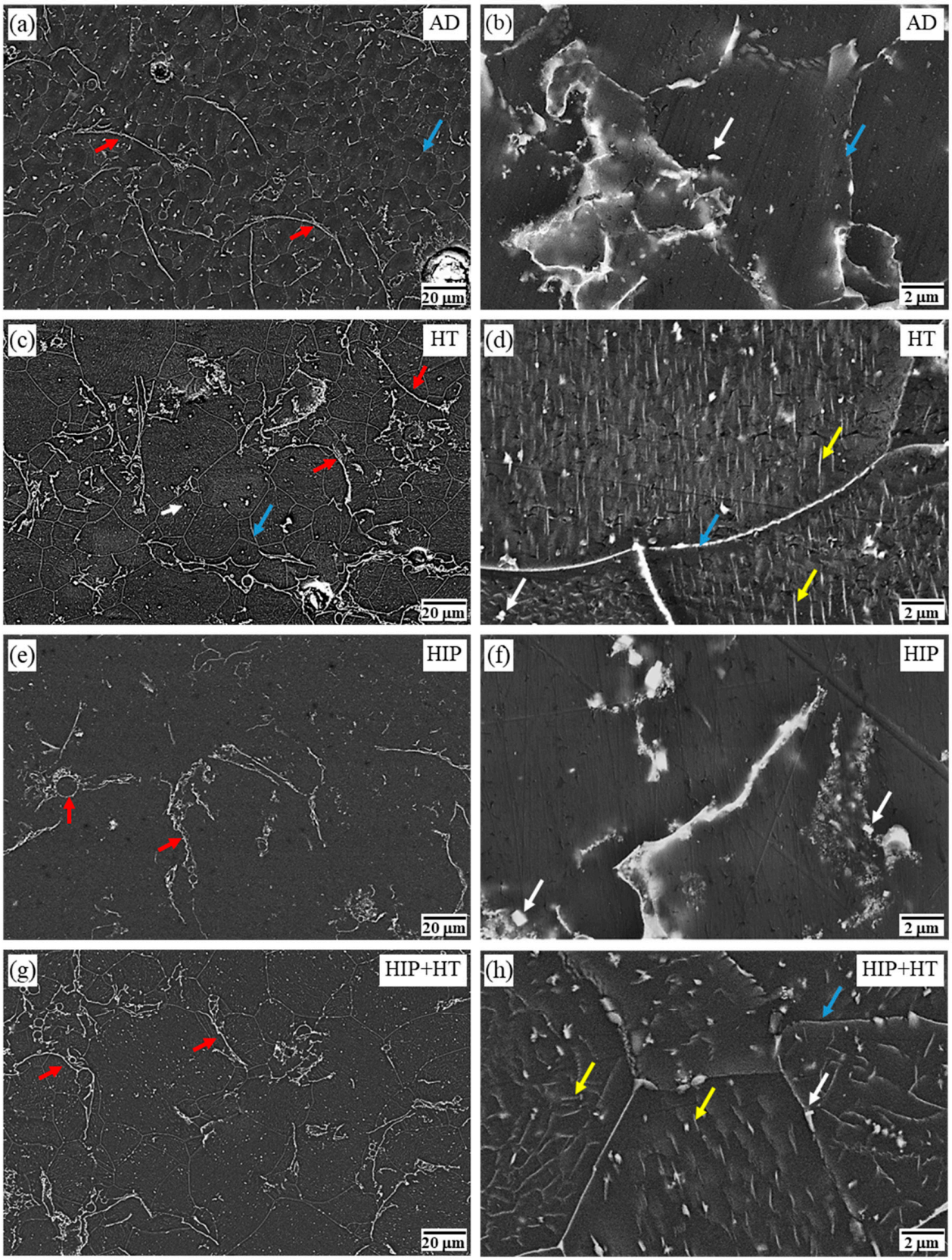

Figure 5. SEM micrographs of additively manufactured WE 43 Mg in (**a**,**b**) AD, (**c**,**d**) HT, (**e**,**f**) HIP, and (**g**,**h**) HIP + HT conditions. The red and blue arrows mark the arc-shape phases and the grain boundary regions, respectively. The white and yellow arrows indicate cuboidal precipitates and needle-like precipitates, respectively.

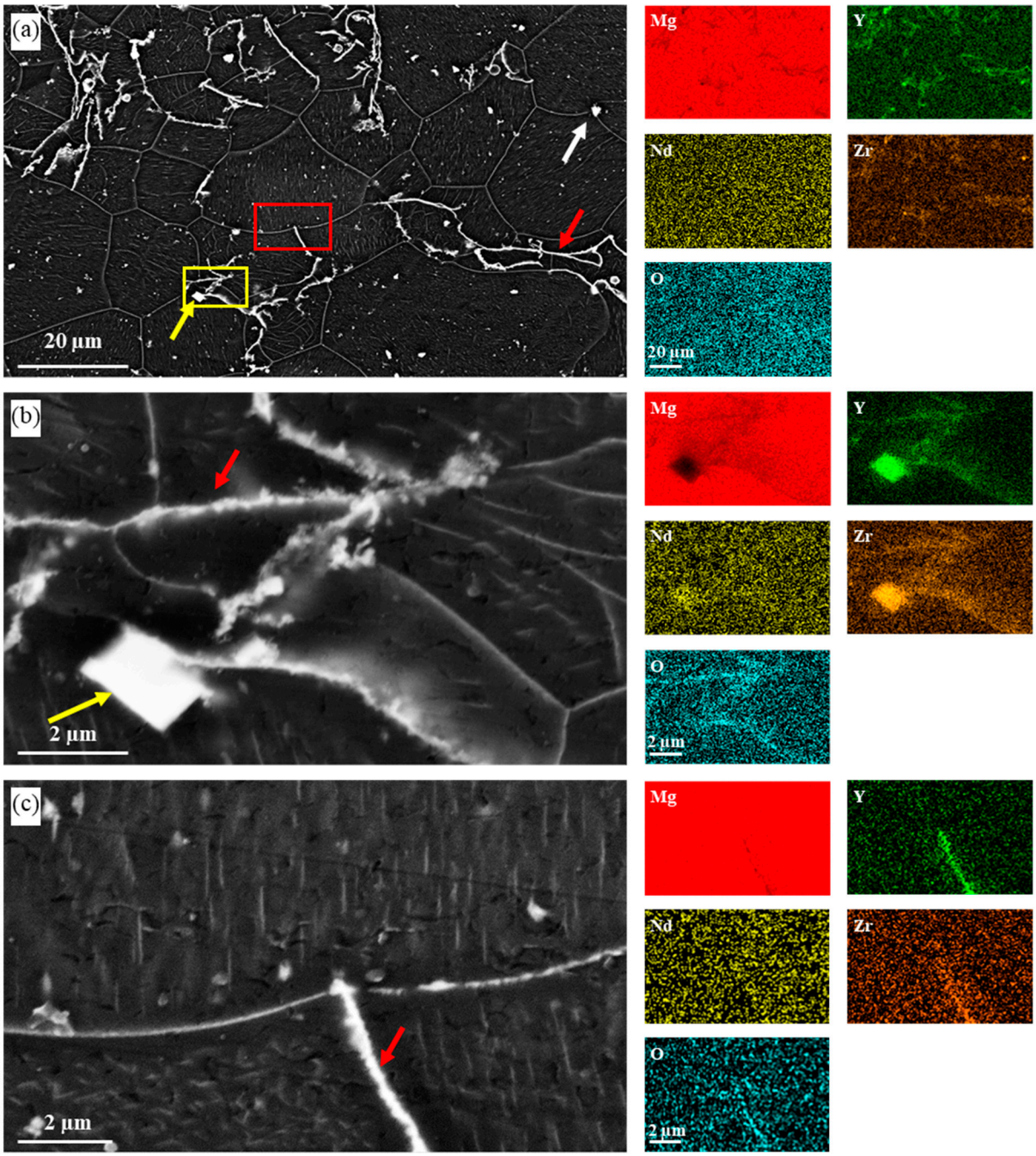

Figure 6. (**a**) low magnification SEM images and corresponding EDS maps of the HT sample. (**b**,**c**) higher magnification SEM images and corresponding EDS maps of the regions marked by yellow and red rectangles, respectively. Red arrows indicate the powder boundaries. Yellow and white arrows indicate the cuboidal and irregular precipitates, respectively.

Figure 7 shows EBSD Euler maps and corresponding pole figures of the LPDED samples in various post-processing conditions. Grain size measurements obtained via EBSD analysis are provided in Table 3 and show an increase in grain size after post-processing, which correlates well with the results obtained using the optical metallography line-intercept method (Table 2). The large standard deviation for the HT and HIP + HT samples has likely occurred due to the presence of AGG. Moreover, by inspection of Figure 7, the microstructure of the samples in all processing conditions consists of an equiaxed-grain structure with random orientations.

Table 3. The grain size of LPDED WE43 Mg specimens in as-deposited and post-processed conditions measured via EBSD.

Sample Condition	Grain Diameter (μm)
AD	9.0 ± 6.4
HT	12.2 ± 9.1
HIP	10.3 ± 5.3
HIP + HT	11.4 ± 8.4

Previously, Jiang et al. [28] have reported an equiaxed-grain structure with random crystallographic orientations and a weak texture for a similar Mg alloy (Mg-9Gd-3Y-0.2Zr) deposited using DED method [28]. Similarly, Liao et al. [51] reported the equiaxed grains with random orientation in the GW103K Mg alloy (Mg-10Gd-3Y-0.4Zr (wt%)) fabricated using the laser-melting deposition technique. However, the previous studies on the EBSD analysis of WE43 Mg fabricated using PBF demonstrated irregular or columnar grain structure [23,29].

Bär et al. [23] demonstrated the presence of three different grain structures in the WE43 samples fabricated using PBF: fine equiaxed-grain structure in the last melt pool; fine columnar structure in the second-to-last layer; and small equiaxed grains dispersed among large irregular grains, with the c-axis parallel to the build direction, in all other layers [23]. In another study, Esmaily et al. [29], reported fine irregular grain structure and strong basal texture with grains parallel to the build direction in the WE43 samples fabricated using SLM. The authors also reported that post processing resulted in subtle grain growth [29]. Specimens fabricated using DED and SLM experience different cooling rates. In the DED processes, the heat transfer primarily occurs through conduction to the substrate or the build material and convection to the gas atmosphere (Ar gas), whereas in SLM, the melt pool is surrounded by the powder, which acts as a thermal insulator and reduces convective heat transfer and lowers the cooling rate, compared with DED [52]. The higher cooling rate of the melt pool in our study results in the fine equiaxed-grain structure.

From inspection of pole figures in Figure 7, it appears that samples in all processing conditions have near random crystal orientation. Moreover, the HIP + HT sample appears to have the strongest texture intensity; however, due to the small sampling region and low count of grains in the mapping area, these results are insufficient for defining the texture of the samples. Inspection of the corresponding pole figure (Figure 7h) shows presence of one preferred texture orientation in the legend of (0001) which can be attributed to the large grain in the Euler map.

Figure 8 shows higher-magnification EBSD Euler maps and corresponding forescatter diode (FSD) images of the samples in various post-processing conditions. Comparing the FSD images and the corresponding EBSD Euler maps, the microstructure of the samples in all processing conditions reveals finer grain structure in the regions adjacent to the arc-shaped phases. This is likely due to the arc-shaped phases acting as heterogeneous nucleation sites during the solidification of the melt pool, leading to the formation of finer grains. Moreover, as was discussed before, EBSD analysis also confirms that the post processing (i.e., HIP, HT, and HIP + HT) resulted in abnormal grain growth (Figures 7c,e,g and 8c,g). However, comparing the EBSD Euler maps and corresponding FSD micrographs (i.e., Figure 8c,d), the areas that the abnormal grain growth (white arrows in Figure 8) mostly occurred in were the regions depleted from the secondary phases (e.g., arc-shaped phases), whereas the presence of arc-shaped phases resulted in smaller grains with insignificant grain growth (marked by white-dashed ovals in Figure 8). This can be attributed to Zener pinning by the arc-shaped phases, which prevents the grain boundary movement and the grain growth during the heat treatment.

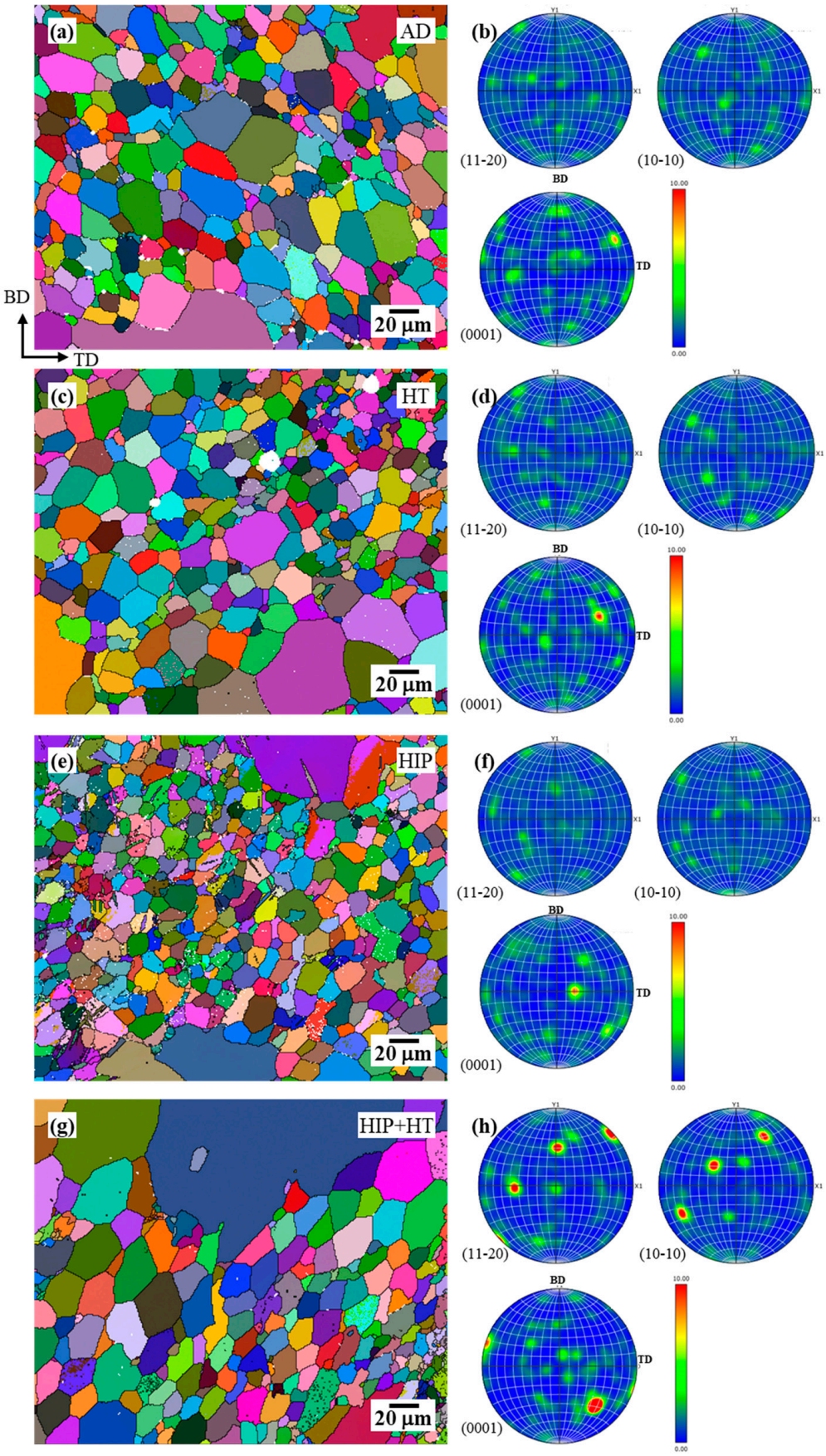

Figure 7. (**a**,**c**,**e**,**g**) EBSD Euler maps and (**b**,**d**,**f**,**h**) corresponding pole figures of additively manufactured WE 43 Mg in (**a**,**b**) AD, (**c**,**d**) HT, (**e**,**f**) HIP, and (**g**,**h**) HIP + HT conditions.

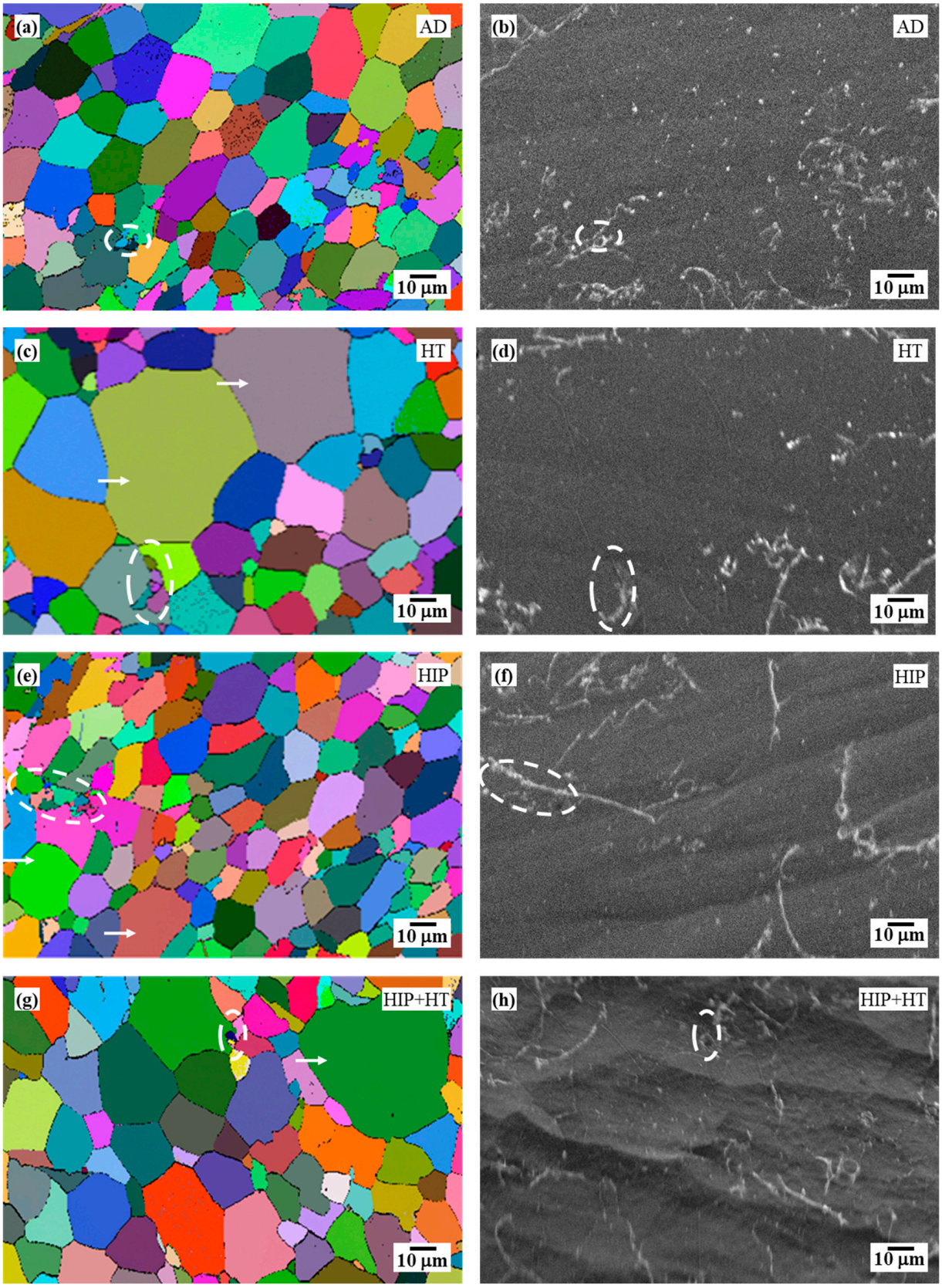

Figure 8. (**a**,**c**,**e**,**g**) EBSD Euler maps and (**b**,**d**,**f**,**h**) corresponding forescatter diode (FSD) micrographs of additively manufactured WE 43 Mg in (**a**,**b**) AD, (**c**,**d**) HT, (**e**,**f**) HIP, and (**g**,**h**) HIP + HT conditions. The white arrows mark the grains with abnormal grain growth. The areas with fine grains and the corresponding regions in the SEM images are marked with the dashed white ovals.

Figure 9 shows high-magnification band contrast and corresponding IPF Z images of the samples in various post-processing conditions obtained using the TKD method. The band-contrast images of samples in HT and HT+HIP confirm the presence of the needle-like precipitates inside the grains. These precipitates were not observed in the AD and HIP samples. Moreover, the IPF Z images in Figure 9b,d,f,h confirm the randomized grain structure in all the samples that were observed using the EBSD method (Figures 7 and 8).

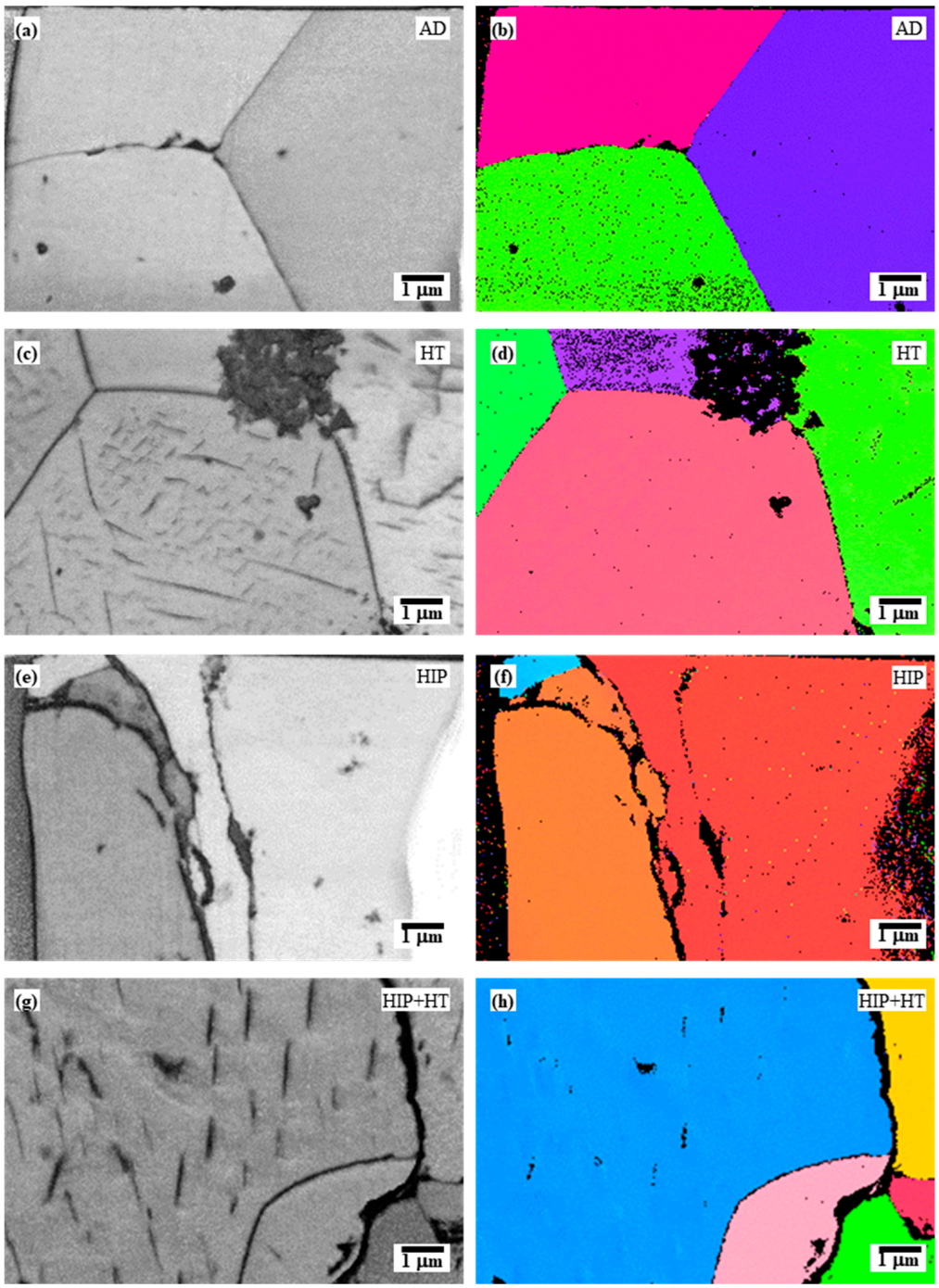

Figure 9. (**a**,**c**,**e**,**g**) Band-contrast and (**b**,**d**,**f**,**h**) IPF Z images of additively manufactured WE 43 Mg in (**a**,**b**) AD, (**c**,**d**) HT, (**e**,**f**) HIP, and (**g**,**h**) HIP + HT conditions created using TKD method.

Figure 10 shows bright-field TEM images of the samples in various post-processing conditions. The bright-field image of the sample in AD condition (Figure 10a) indicates the presence of small grain boundary precipitates and some needle-like precipitates within the grains. However, after HIP processing (Figure 10c), the grain boundary precipitates appear to have dissolved. Further, HT and HIP + HT specimens (yellow arrows in Figure 10b,d) exhibited grain boundary precipitates and the formation of needle-like precipitates. TEM analysis also revealed the presence of arc-shape phases and small unmelted satellite particles (~1 µm in diameter) contained within all samples (only shown for HIP sample in Figure 10c).

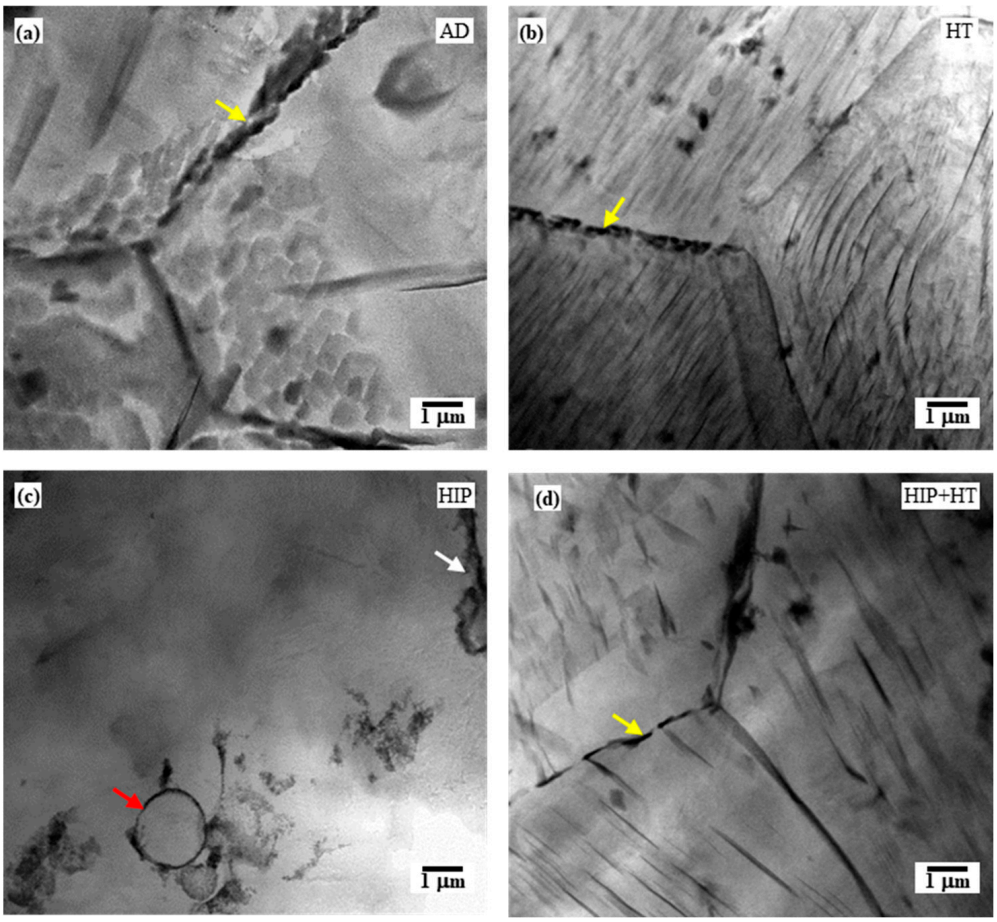

Figure 10. (**a**–**d**) TEM bright-field images of precipitates of additively manufactured WE 43 Mg in (**a**) AD, (**b**) HT, (**c**) HIP, and (**d**) HIP + HT conditions. The yellow, red, and white arrows mark the grain boundary precipitates, unmelted particles, and the arc-shaped phases, respectively.

Figure 11 shows bright-field TEM images and corresponding SAED patterns obtained from the HIP + HT sample. From inspection of Figure 11a,b, two precipitate morphologies are present in the HIP + HT microstructure: needle-like and globular. Here, the needle-like precipitates are approximately 800–1000 nm in length and roughly 10–50 nm in width. The globular precipitates range in size from 100 to 200 nm. Figure 11b shows a higher-magnification image of these precipitates. In this image, the globular precipitates are found attached to the needle-like precipitates. The SAED patterns in Figures 11e and 11f, respectively, show a rhombus and a hexagonal diffraction pattern associated with the HCP α-Mg lattice. In both SAED patterns, weak diffraction spots, located between α-Mg diffraction spots, are observed and are attributed to the precipitates formed during heat-treatment process (β_1 or β). During the aging of WE43, precipitates form from the Mg supersaturated solid solution ((Mg)S.S.S.S), as follows: (Mg)S.S.S.S→β″→β′→β_1→β [48,53]. Here, β″ (Mg_3Nd

or $Mg_3(Y_{0.85}Nd_{0.15})$) is a coherent metastable secondary phase with HCP $D0_{19}$ crystal structure with a double hexagonal cell (a = $2a_{Mg}$ = 0.6418 nm, c = c_{Mg} = 0.521 nm) [48,50,54]. β″ phase precipitates are plate-shaped precipitates that lie in the $(1\bar{1}00)$ Mg planes [47,50]. This phase can transform to β′ ($Mg_{12}NdY$ or $Mg_{24}Y_2Nd_3$) at temperatures around 200 to 250 °C. β′ is a semicoherent globular base-centered orthorhombic (BCO) metastable phase (a = $2a_{Mg}$= 0.640nm, b = $8d_{Mg(1\bar{1}00)}$ = 2.223 nm, c = c_{Mg}= 0.521 nm) [47,48,54]. Finally, β_1 is an intermediate phase that can also form with β′ and is often connected to the globular β′ phase. This phase (β_1) typically takes on a plate-like morphology and forms on the $(1\bar{1}00)$ Mg planes with a face-centered cubic (FCC) crystal structure and a crystal size of a = 0.740 nm [46,47,54]. Mg_3(Nd, Y, Gd) [48] and $Mg_{14}Nd_2Y$ have been suggested [47] as the composition of β_1. The final precipitate to form during aging is a stable FCC longitudinal plate-like β phase with a crystal length of a = 2.223 nm and suggested composition of $Mg_{12}NdY$ [47] (although $Mg_{14}Nd_2Y$ [48] has also been observed). Moreover, it should be noted that the absence of diffraction spots correlating to the other phases (e.g., cuboidal precipitates and arc-shaped phases) in SAED patterns has been attributed to the incoherency of these precipitates with the α-Mg phase [20].

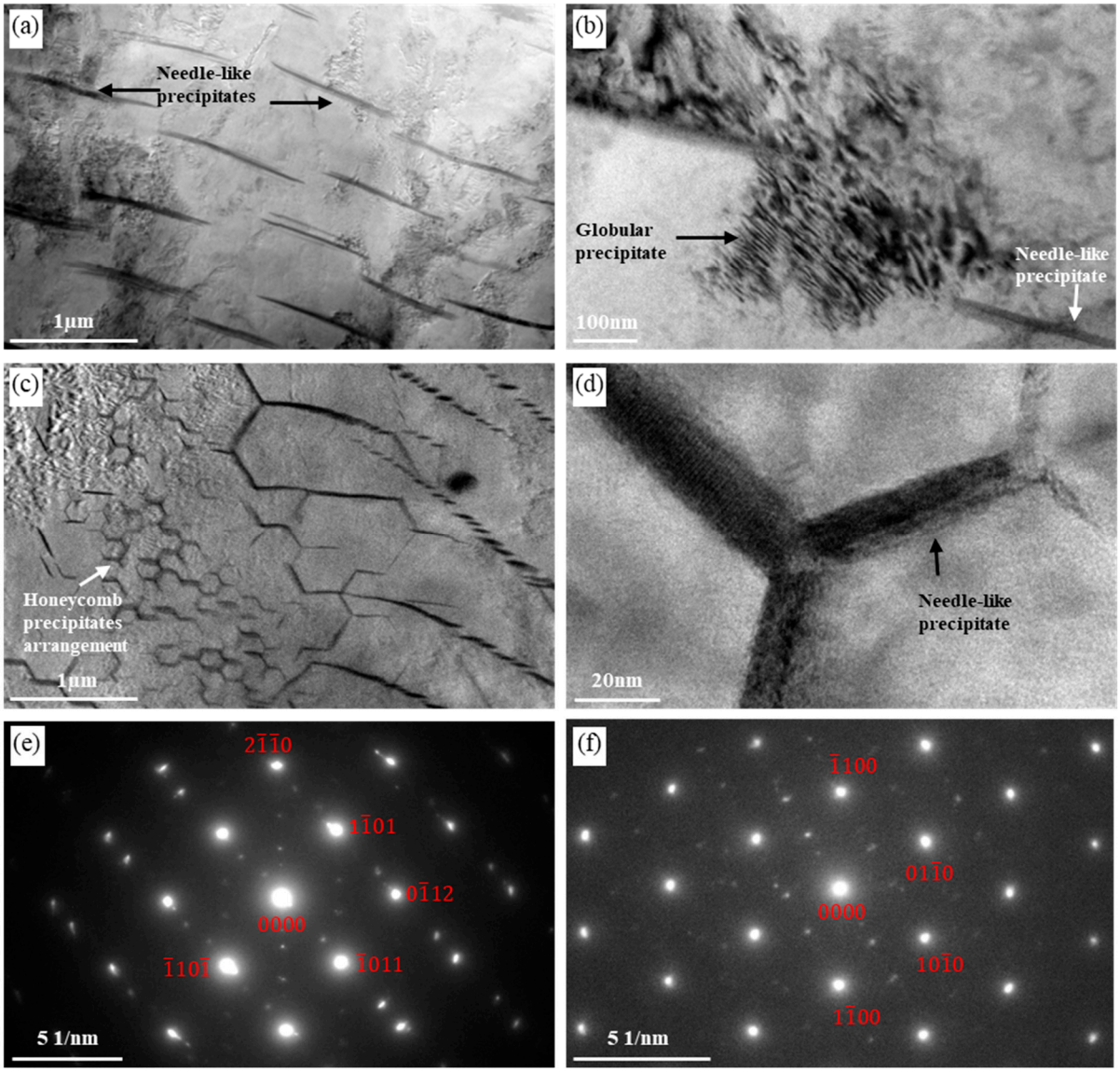

Figure 11. (**a**–**d**) TEM bright field images of precipitates and (**e**,**f**) corresponding SAED pattern of HIP + HT sample taken with the beam direction parallel to (**a**,**b**,**e**) $[01\bar{1}1]$ and (**c**,**d**,**f**) [0001].

To study the composition of the needle-like precipitates, EDS in conjunction with STEM was performed on the HT sample (Figure 12). Inspection of Figure 12 shows that the needle-like precipitates are enriched in Nd and Y, which matches the suggested compositions for the β_1 or β precipitates [47,48]. Therefore, based on the results of TEM and EDS analysis, the needle-like precipitates observed in this study are expected to be either β_1 or β precipitates with plate-like morphology. These two phases can exist in the microstructure simultaneously, although long aging times result in the transformation of the β_1 to the β phase [55,56]. It has been reported that both phases can exist in the same plate-like precipitate in such a way that one end is β_1 while the other end has transformed to the β phase [55,56]. However, the β phase is typically longer and thicker than the β_1 phase. In this study, the thickness and length of needle-like precipitates (i.e., 10–50 nm and 800–1000 nm, respectively) are much smaller than those reported for the β phase (i.e., 250 nm thick and several microns long [47]) and more similar to the thickness and length reported for the β_1 phase (i.e., 20 nm and 200–500 nm, respectively). As such, we believe the needle-like precipitates are most consistent with the β_1 phase. However, the slightly larger size of the needle-like precipitates compared to the β_1 phase may be attributed to overaging, resulting from excessive aging times or temperatures. Moreover, it is possible that the AM samples respond differently to heat treatment than conventional cast alloys, due to differences in thermal history. During LPDED, various regions of the sample experience different thermal history (e.g., heat-affected zones and re-melting regions), which results in the differences in the microstructure [23,52,57].

Figure 11c shows a bright-field TEM image obtained from a different region of the HIP + HT sample. Clearly, the size and orientation of the precipitates in the specimen is not uniform. In this case, the plate-like β_1 precipitates take on a unique honeycomb or triad arrangement, aligned in three primary orientations. Figure 11d shows a higher-magnification bright-field image of one of the triads. Three precipitates intersect at the apex of the triad and are orientated with a 120° separation from one another. The arrangement corresponds to the growth of β_1 precipitates on prismatic planes and along the $< 11\bar{2}0 >$ direction in the α-Mg lattice. This finding has been reported previously in hot-rolled WE43 [58] and peak-aged WE54 plates [56,59] and attributed to the shear strain during the formation of the precipitates. Occasionally, this triad arrangement can also develop into a honeycomb arrangement. Previously, a honeycomb arrangement of β_1 precipitates was reported in hot-rolled and aged (at 210 °C for 48 h) WE43 [58] and solution-treated and aged at 250 °C (16 h [55] and 10 h [60]) WE54 plates. Finally, the variation in precipitate size and distribution observed in the HIP + HT specimen may indicate that the response of the LPDED material to heat treatment was non-uniform, owing to the variation in local- and global-temperature profiles during deposition, and associated solute-element segregation in various regions (e.g., regions which experience re-melting) of the AD material.

Figure 12e,f show high-magnification SEM image and corresponding EDS map of the HT sample. From these images, it can be noticed that the grain boundary precipitates are rich in Nd and Y. These images also show that the powder boundary oxide phases are composed of small oxide particles that are aggregated together.

The XRD patterns of the WE43 powder and four LPDED sample treatments are provided in Figure 13. The predominant diffraction peaks for each pattern are characteristic of α-Mg. In addition, peaks are present in each pattern which can be attributed to secondary phases such as $Mg_{24}Y_5$, $Mg_{12}Nd$, and $Mg_{41}Nd_5$. The peaks related to the yttrium oxide (Y_2O_3) and zirconium oxide (Zr_3O_{1-x}) were also observed in all processing conditions and were attributed to the oxide layer on the surface of the powder and associated arc-shaped phases observed in the LPDED specimens.

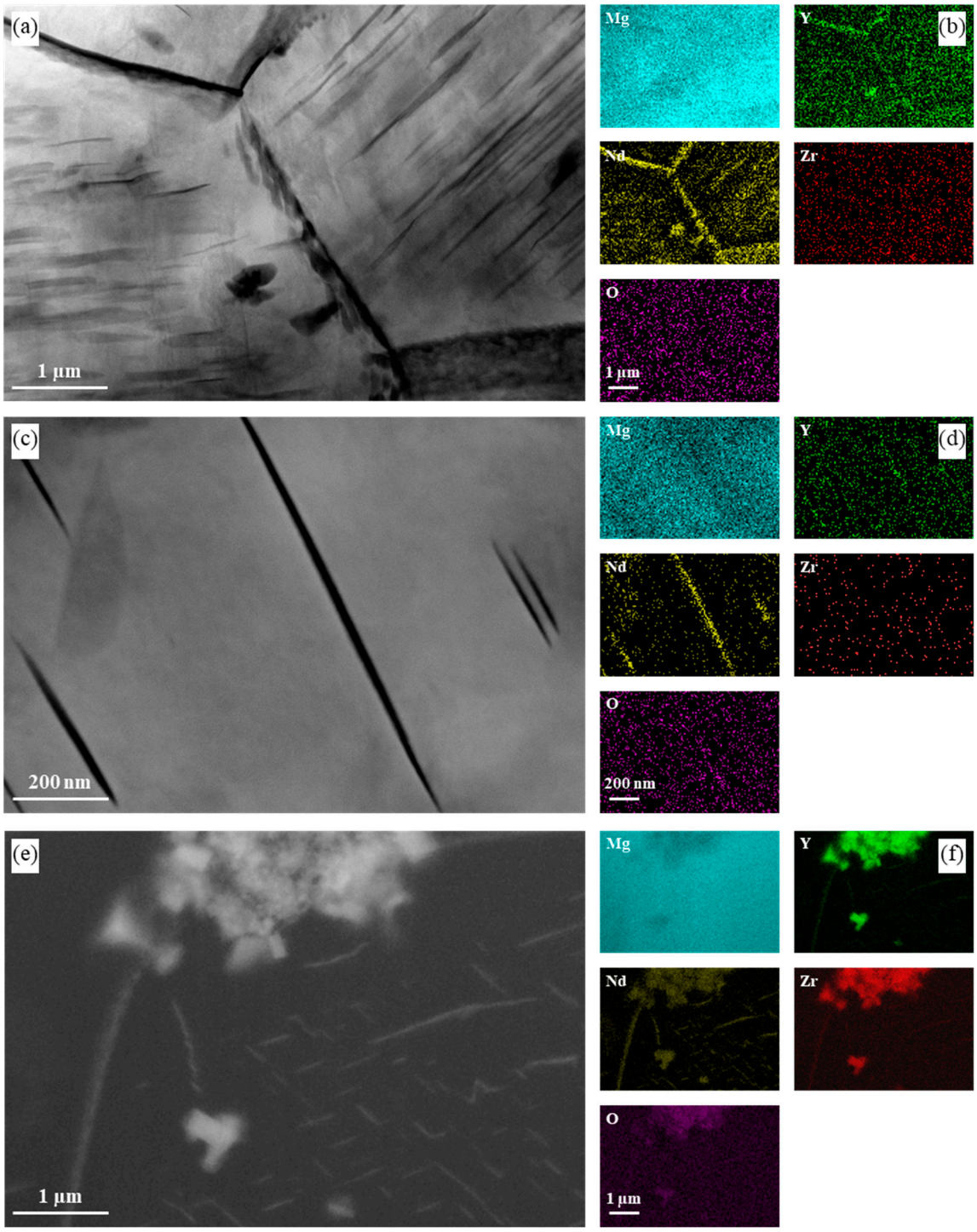

Figure 12. (**a**,**c**) STEM and (**e**) SEM images and (**b**,**d**,**f**) corresponding EDS maps of the HT sample.

Further inspection of Figure 13 shows that peaks corresponding to $Mg_{12}Nd$ (marked by a blue diamond) are only present in the feedstock powder. This phase is the eutectic phase in the Mg-Nd-Y alloys, which dissolves during solution treatment. The absence of $Mg_{12}Nd$ peaks in the XRD pattern of AD samples can be attributed to the small size and volume fraction of the grain-boundary eutectic phase. Moreover, peaks corresponding to the $Mg_{24}Y_5$ phase (cuboidal precipitates in Figure 6) or $Mg_{41}Nd_5$ were not observed in the powder XRD pattern. The absence of these phases is in agreement with the cross-sectional image of the powder, where no precipitation aside from the eutectic phase was observed. Moreover, comparing the XRD pattern of the heat-treated samples (i.e., HT and HIP + HT)

to those without heat treatment (i.e., AD and HIP), the peaks attributed to Mg_3(Nd, Gd, Y), which is the suggested composition for needle-like β_1 precipitates, were present in the HT and HIP + HT diffraction patterns. Furthermore, the HIP XRD pattern did not show the presence of peaks corresponding to either the eutectic phase ($Mg_{12}Nd$) or β_1 phase (Mg_3(Nd, Gd, Y)), which agrees with microstructural observations (Figure 5e).

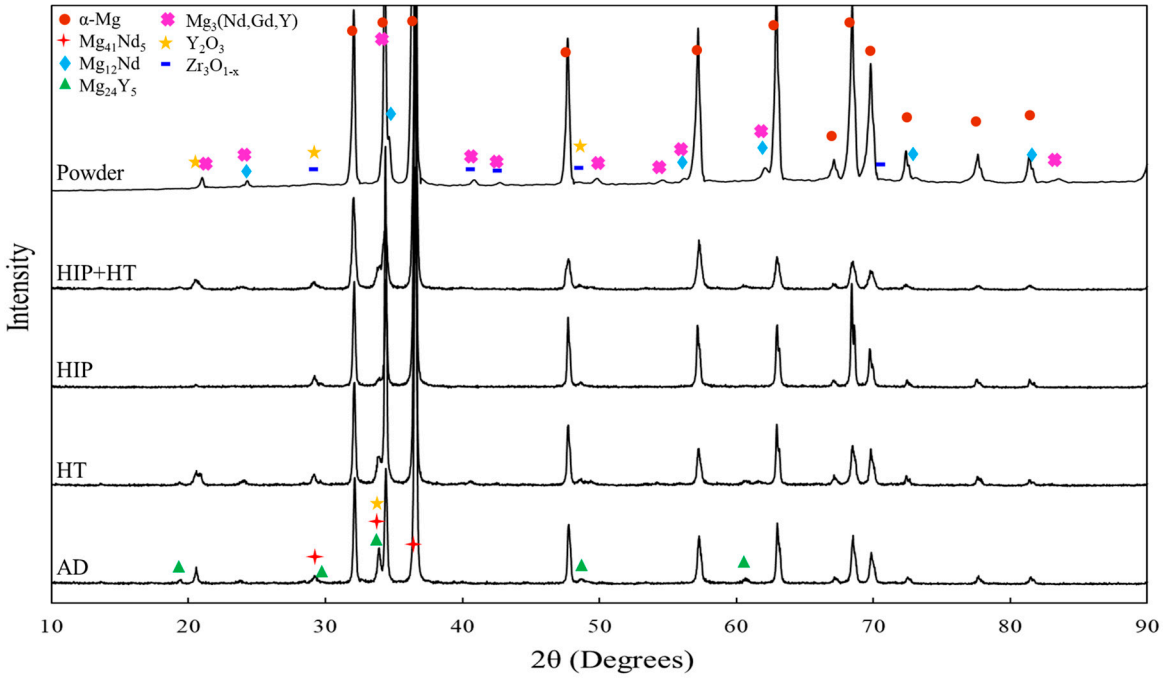

Figure 13. XRD diffraction pattern of the powder and additively manufactured WE43 Mg alloy with different post-processing.

4. Conclusions

LPDED was successfully used to deposit rectangular specimens measuring up to 11 cm in height, with less than 2% porosity in the AD condition. The porosity was significantly decreased by HIP treatment. Furthermore, while limited grain growth occurred as a result of post-deposition heat treatment, abnormal grain growth was observed, which was attributed to the Zener pinning of the grain boundaries. Additionally, EBSD results showed that the microstructure consisted of equiaxed grains with random orientation where abnormal grain growth during post-processing occurred on the regions that were depleted from the secondary phases (e.g., arc-shaped phases) and the presence of the arc-shaped phases resulted in a finer grain structure. Moreover, during the heat treatment, the grain boundary precipitates underwent dissolution and, also, a fine distribution of needle-like precipitates formed, which were identified as β_1 or β phase. TEM evaluation revealed the presence of globular β' phases located at the end of the needle-like precipitates. In addition, some regions of the HIP + HT microstructure showed a honeycomb arrangement of β_1 precipitates and a significant variation in precipitate size and distribution was observed. The non-uniformity of the precipitates may indicate the variation in the thermal history of the different regions of the sample during the LPDED and the response of the various regions of the deposited samples to heat treatment. Moreover, cuboidal Y-rich precipitates and irregular Zr-rich precipitates were present in all additively manufactured samples. The microstructure of LPDED samples in all conditions contained some arc-shaped phases that were rich in Y, O, and Zr. These phases were attributed to the oxide passive layer which was formed on the powder feedstock during production. The exact nature of these

precipitates, however, and their influence on the mechanical and corrosion behavior of the build should be determined in subsequent studies.

Based on the results of this study, the HIP + HT has the most impact on the microstructure of the samples, by not only reducing the porosity, but also the formation, of dispersed needle-like precipitates. However, to determine the optimal post-processing method for the AM Mg, the effect of post processing on the mechanical behavior and corrosion behavior of the samples should also be investigated.

Author Contributions: Conceptualization, L.S. and G.A.C.; methodology, L.S. and G.A.C.; investigation, L.S. and N.J.M.; data curation, L.S. and N.J.M.; writing—original draft preparation, L.S.; writing—review and editing, N.J.M. and G.A.C.; supervision, G.A.C.; project administration, G.A.C.; funding acquisition, G.A.C. All authors have read and agreed to the published version of the manuscript.

Funding: This research was funded by the South Dakota Board of Regents under the auspices of the Surface Engineering Research Center (SERC).

Data Availability Statement: The original contributions presented in this study are included in the article. Further inquiries can be directed to the corresponding author.

Acknowledgments: The authors would like to express their sincere gratitude to Magnus Ahlfors, Chad Beamer, and Quintus Technologies, LLC for performing the hot isostatic press. The authors also wish to thank Scott P. Ahrenkiel for performing the TEM imaging.

Conflicts of Interest: The authors declare no conflicts of interest.

References

1. Chen, Y.; Xu, Z.; Smith, C.; Sankar, J. Recent advances on the development of magnesium alloys for biodegradable implants. *Acta Biomater.* **2014**, *10*, 4561–4573. [CrossRef]
2. Witte, F. The history of biodegradable magnesium implants: A review. *Acta Biomater.* **2010**, *6*, 1680–1692. [CrossRef]
3. Gill, P.; Munroe, N. Review on magnesium alloys as biodegradable implant materials. *Int. J. Biomed. Eng. Technol.* **2012**, *10*, 383–398. [CrossRef]
4. Heublein, B.; Rohde, R.; Kaese, V.; Niemeyer, M.; Hartung, W.; Haverich, A. Biocorrosion of magnesium alloys: A new principle in cardiovascular implant technology? *Heart* **2003**, *89*, 651–656. [CrossRef]
5. Akbarzadeh, F.Z.; Sarraf, M.; Ghomi, E.R.; Kumar, V.V.; Salehi, M.; Ramakrishna, S.; Bae, S. A state-of-the-art review on recent advances in the fabrication and characteristics of magnesium-based alloys in biomedical applications. *J. Magnes. Alloys* **2024**, *12*, 2569–2594. [CrossRef]
6. Esmaily, M.; Svensson, J.; Fajardo, S.; Birbilis, N.; Frankel, G.; Virtanen, S.; Arrabal, R.; Thomas, S.; Johansson, L. Fundamentals and advances in magnesium alloy corrosion. *Prog. Mater. Sci.* **2017**, *89*, 92–193. [CrossRef]
7. Agarwal, S.; Curtin, J.; Duffy, B.; Jaiswal, S. Biodegradable magnesium alloys for orthopaedic applications: A review on corrosion, biocompatibility and surface modifications. *Mater. Sci. Eng. C* **2016**, *68*, 948–963. [CrossRef]
8. Kaushik, V.; Kumar, N.; Vignesh, M. Magnesium role in additive manufacturing of biomedical implants–challenges and opportunities. *Addit. Manuf.* **2022**, *55*, 102802.
9. Manakari, V.; Parande, G.; Gupta, M. Selective laser melting of magnesium and magnesium alloy powders: A review. *Metals* **2016**, *7*, 2. [CrossRef]
10. Wei, K.; Gao, M.; Wang, Z.; Zeng, X. Effect of energy input on formability, microstructure and mechanical properties of selective laser melted AZ91D magnesium alloy. *Mater. Sci. Eng. A* **2014**, *611*, 212–222. [CrossRef]
11. Karunakaran, R.; Ortgies, S.; Tamayol, A.; Bobaru, F.; Sealy, M.P. Additive manufacturing of magnesium alloys. *Bioact. Mater.* **2020**, *5*, 44–54. [CrossRef] [PubMed]
12. Sezer, N.; Evis, Z.; Koc, M. Additive manufacturing of biodegradable magnesium implants and scaffolds: Review of the recent advances and research trends. *J. Magnes. Alloys* **2021**, *9*, 392–415. [CrossRef]
13. Li, Y.; Zhou, J.; Pavanram, P.; Leeflang, M.; Fockaert, L.; Pouran, B.; Tümer, N.; Schröder, K.-U.; Mol, J.; Weinans, H. Additively manufactured biodegradable porous magnesium. *Acta Biomater.* **2018**, *67*, 378–392. [CrossRef] [PubMed]
14. Larimian, T.; Kannan, M.; Grzesiak, D.; AlMangour, B.; Borkar, T. Effect of energy density and scanning strategy on densification, microstructure and mechanical properties of 316L stainless steel processed via selective laser melting. *Mater. Sci. Eng. A* **2020**, *770*, 138455. [CrossRef]

15. Long, T.; Zhang, X.; Huang, Q.; Liu, L.; Liu, Y.; Ren, J.; Yin, Y.; Wu, D.; Wu, H. Novel Mg-based alloys by selective laser melting for biomedical applications: Microstructure evolution, microhardness and in vitro degradation behaviour. *Virtual Phys. Prototyp.* **2018**, *13*, 71–81. [CrossRef]
16. Ng, C.; Savalani, M.; Man, H.; Gibson, I. Layer manufacturing of magnesium and its alloy structures for future applications. *Virtual Phys. Prototyp.* **2010**, *5*, 13–19. [CrossRef]
17. Tandon, R.; Wilks, T.; Gieseke, D.I.M.; Noelke, D.I.C.; Kaierle, S.; Palmer, T. Additive manufacturing of electron® 43 alloy using laser powder bed and directed energy deposition. In Proceedings of the International Power Metallurgy Congress and Exhibition, European PM Conference Proceedings, Reims, France, 4–7 October 2015.
18. Zhang, M.; Chen, C.; Liu, C.; Wang, S. Study on Porous Mg-Zn-Zr ZK61 Alloys Produced by Laser Additive Manufacturing. *Metals* **2018**, *8*, 635. [CrossRef]
19. Tandon, R.; Palmer, T.; Gieseke, M.; Noelke, C.; Kaierle, S. Additive Manufacturing of Magnesium Alloy Powders: Investigations Into Process Development Using Elektron® MAP + 43 Via Laser Powder Bed Fusion and Directed Energy Deposition. In Proceedings of the European Congress and Exhibition on Powder Metallurgy. European PM Conference Proceedings, Hamburg, Germany, 13 October 2016; pp. 1–6.
20. Gangireddy, S.; Gwalani, B.; Liu, K.; Faierson, E.J.; Mishra, R.S. Microstructure and mechanical behavior of an additive manufactured (AM) WE43-Mg alloy. *Addit. Manuf.* **2019**, *26*, 53–64. [CrossRef]
21. Yang, Y.; Wu, P.; Wang, Q.; Wu, H.; Liu, Y.; Deng, Y.; Zhou, Y.; Shuai, C. The enhancement of Mg corrosion resistance by alloying Mn and laser-melting. *Materials* **2016**, *9*, 216. [CrossRef] [PubMed]
22. Li, Y.; Jahr, H.; Zhang, X.; Leeflang, M.; Li, W.; Pouran, B.; Tichelaar, F.; Weinans, H.; Zhou, J.; Zadpoor, A. Biodegradation-affected fatigue behavior of additively manufactured porous magnesium. *Addit. Manuf.* **2019**, *28*, 299–311. [CrossRef]
23. Bär, F.; Berger, L.; Jauer, L.; Kurtuldu, G.; Schäublin, R.; Schleifenbaum, J.H.; Löffler, J.F. Laser additive manufacturing of biodegradable magnesium alloy WE43: A detailed microstructure analysis. *Acta Biomater.* **2019**, *98*, 36–49. [CrossRef]
24. Zeng, Z.; Salehi, M.; Kopp, A.; Xu, S.; Esmaily, M.; Birbilis, N. Recent progress and perspectives in additive manufacturing of magnesium alloys. *J. Magnes. Alloys* **2022**, *10*, 1511–1541. [CrossRef]
25. Julmi, S.; Abel, A.; Gerdes, N.; Hoff, C.; Hermsdorf, J.; Overmeyer, L.; Klose, C.; Maier, H.J. Development of a laser powder bed fusion process tailored for the additive manufacturing of high-quality components made of the commercial magnesium alloy WE43. *Materials* **2021**, *14*, 887. [CrossRef]
26. Xu, W.; Li, J.; Zhang, Z.; Yuan, H.; An, G.; Shi, H.; Cai, C.; Jiang, W.; Li, W.; Wei, Q. Laser powder bed fusion of WE43 magnesium alloy with superior balance of strength and ductility. *J. Magnes. Alloys* **2024**. [CrossRef]
27. Motallebi, R.; Savaedi, Z.; Mirzadeh, H. Post-processing heat treatment of lightweight magnesium alloys fabricated by additive manufacturing: A review. *J. Mater. Res. Technol.* **2022**, *20*, 1873–1892. [CrossRef]
28. Jiang, Y.; Tang, H.; Li, Z.; Zheng, D.; Tu, Y. Additive manufactured Mg-Gd-Y-Zr alloys: Effects of Gd content on microstructure evolution and mechanical properties. *Addit. Manuf.* **2022**, *59*, 103136. [CrossRef]
29. Esmaily, M.; Zeng, Z.; Mortazavi, A.; Gullino, A.; Choudhary, S.; Derra, T.; Benn, F.; D'Elia, F.; Müther, M.; Thomas, S. A detailed microstructural and corrosion analysis of magnesium alloy WE43 manufactured by selective laser melting. *Addit. Manuf.* **2020**, *35*, 101321. [CrossRef]
30. Sorkhi, L.; Hammell, J.J.; Crawford, G.A. Effect of Interlayer Interval Time on the Microstructure and Mechanical Behavior of Additively Manufactured WE43 Mg Alloy. *Metall. Mater. Trans. A* **2020**, *51*, 4390–4405. [CrossRef]
31. Avedesian, M.M.; Baker, H. *ASM Specialty Handbook: Magnesium and Magnesium Alloys*, 2nd ed.; ASM International: Almere, The Netherlands, 1999.
32. *ASTM E2109-01*; Test Methods for Determining Area Percentage Porosity in Thermal Sprayed Coatings. ASTM West Conshohocken: West Conshohocken, PA, USA, 2014.
33. Voort, V.; George, F. *Metallography, Principles and Practice*; ASM International: Almere, The Netherlands, 1999; Volume 487.
34. *ASTM E112*; Standard Test Methods for Determining Average Grain Size. ASTM West Conshohocken: West Conshohocken, PA, USA, 2004.
35. Attar, H.; Bermingham, M.; Ehtemam-Haghighi, S.; Dehghan-Manshadi, A.; Kent, D.; Dargusch, M. Evaluation of the mechanical and wear properties of titanium produced by three different additive manufacturing methods for biomedical application. *Mater. Sci. Eng. A* **2019**, *760*, 339–345. [CrossRef]
36. Tandon, R.; Madan, D. Emerging applications for magnesium alloy powders. *Powder Metall.* **2014**, *57*, 236–241. [CrossRef]
37. Humphreys, F.J.; Hatherly, M. *Recrystallization and Related Annealing Phenomena*; Elsevier: Amsterdam, The Netherlands, 2012.
38. Hillert, M. On the theory of normal and abnormal grain growth. *Acta Met.* **1965**, *13*, 227–238. [CrossRef]
39. Bhattacharyya, J.J.; Agnew, S.; Muralidharan, G. Texture enhancement during grain growth of magnesium alloy AZ31B. *Acta Mater.* **2015**, *86*, 80–94. [CrossRef]
40. Rollett, A.; Srolovitz, D.J.; Anderson, M. Simulation and theory of abnormal grain growth—Anisotropic grain boundary energies and mobilities. *Acta Met.* **1989**, *37*, 1227–1240. [CrossRef]

41. Beck, P.A.; Sperry, P.R. Efeet of recrystallization texture on grain growth. *JOM* **1949**, *1*, 240–241. [CrossRef]
42. Abrivard, G.; Busso, E.P.; Forest, S.; Appolaire, B. Phase field modelling of grain boundary motion driven by curvature and stored energy gradients. Part I: Theory and numerical implementation. *Philos. Mag.* **2012**, *92*, 3618–3642. [CrossRef]
43. Gerber, P.; Tarasiuk, J.; Chauveau, T.; Bacroix, B. A quantitative analysis of the evolution of texture and stored energy during annealing of cold rolled copper. *Acta Mater.* **2003**, *51*, 6359–6371. [CrossRef]
44. Roostaei, M.; Shirdel, M.; Parsa, M.; Mahmudi, R.; Mirzadeh, H. Microstructural evolution and grain growth kinetics of GZ31 magnesium alloy. *Mater. Charact.* **2016**, *118*, 584–592. [CrossRef]
45. Tammas-Williams, S.; Withers, P.; Todd, I.; Prangnell, P. Porosity regrowth during heat treatment of hot isostatically pressed additively manufactured titanium components. *Scr. Mater.* **2016**, *122*, 72–76. [CrossRef]
46. Jiang, H.; Zheng, M.; Qiao, X.; Wu, K.; Peng, Q.; Yang, S.; Yuan, Y.; Luo, J. Microstructure and mechanical properties of WE43 magnesium alloy fabricated by direct-chill casting. *Mater. Sci. Eng. A* **2017**, *684*, 158–164. [CrossRef]
47. Kang, Y.H.; Yan, H.; Chen, R.S. Effects of heat treatment on the precipitates and mechanical properties of sand-cast Mg–4Y–2.3 Nd–1Gd–0.6 Zr magnesium alloy. *Mater. Sci. Eng. A* **2015**, *645*, 361–368. [CrossRef]
48. Rzychoń, T.; Kiełbus, A. Microstructure of WE43 casting magnesium alloys. *J. Achiev. Mater. Manuf. Eng.* **2007**, *21*, 31–34.
49. Ning, Z.; Yi, J.; Qian, M.; Sun, H.; Cao, F.; Liu, H.; Sun, J. Microstructure and elevated temperature mechanical and creep properties of Mg–4Y–3Nd–0.5 Zr alloy in the product form of a large structural casting. *Mater. Des.* **2014**, *60*, 218–225. [CrossRef]
50. Tian, Z.; Yang, Q.; Guan, K.; Meng, J.; Cao, Z. Microstructure and mechanical properties of a peak-aged Mg-5Y-2.5 Nd-1.5 Gd-0.5 Zr casting alloy. *J. Alloy. Compd.* **2018**, *731*, 704–713. [CrossRef]
51. Liao, H.; Fu, P.; Peng, L.; Li, J.; Zhang, S.; Hu, G.; Ding, W. Microstructure and mechanical properties of laser melting deposited GW103K Mg-RE alloy. *Mater. Sci. Eng. A* **2017**, *687*, 281–287. [CrossRef]
52. Sames, W.J.; List, F.; Pannala, S.; Dehoff, R.R.; Babu, S.S. The metallurgy and processing science of metal additive manufacturing. *Int. Mater. Rev.* **2016**, *61*, 315–360. [CrossRef]
53. Li, H.; Lv, F.; Liang, X.; Qi, Y.; Zhu, Z.; Zhang, K. Effect of heat treatment on microstructures and mechanical properties of a cast Mg-Y-Nd-Zr alloy. *Mater. Sci. Eng. A* **2016**, *667*, 409–416. [CrossRef]
54. Antion, C.; Donnadieu, P.; Perrard, F.; Deschamps, A.; Tassin, C.; Pisch, A. Hardening precipitation in a Mg–4Y–3RE alloy. *Acta Mater.* **2003**, *51*, 5335–5348. [CrossRef]
55. Xu, Z.; Weyland, M.; Nie, J. On the strain accommodation of β1 precipitates in magnesium alloy WE54. *Acta Mater.* **2014**, *75*, 122–133. [CrossRef]
56. Nie, J.F.; Muddle, B.C. Characterisation of strengthening precipitate phases in a Mg–Y–Nd alloy. *Acta Mater.* **2000**, *48*, 1691–1703. [CrossRef]
57. Thompson, S.M.; Bian, L.; Shamsaei, N.; Yadollahi, A. An overview of Direct Laser Deposition for additive manufacturing; Part I: Transport phenomena, modeling and diagnostics. *Addit. Manuf.* **2015**, *8*, 36–62. [CrossRef]
58. Choudhuri, D.; Meher, S.; Nag, S.; Dendge, N.; Hwang, J.; Banerjee, R. Evolution of a honeycomb network of precipitates in a hot-rolled commercial Mg–Y–Nd–Zr alloy. *Philos. Mag. Lett.* **2013**, *93*, 395–404. [CrossRef]
59. Nie, J.F. Precipitation and hardening in magnesium alloys. *Metall. Mater. Trans. A* **2012**, *43*, 3891–3939. [CrossRef]
60. Liu, H.; Gao, Y.; Xu, Z.; Zhu, Y.; Wang, Y.; Nie, J. Guided self-assembly of nano-precipitates into mesocrystals. *Sci. Rep.* **2015**, *5*, 16530. [CrossRef]